

# ALGORITHM THEORETICAL BASIS DOCUMENT

## IASI Dust

(O3M-372, O3M-430)

Prepared by	Lieven Clarisse Daniel Hurtmans Rosa Astoreca Pierre-François Coheur Juliette Hadji-Lazaro Sarah Safieddine Cathy Clerbaux	December 10 <sup>th</sup> , 2024
-------------	--	----------------------------------

**DOCUMENT STATUS SHEET**

<b>Issue</b>	<b>Date</b>	<b>Modified items / reason for change</b>
1.0	05/10/2021	First version of the IASI Dust product ATBD
1.1	14/02/2022	Updates of the document following MTR reviewer's comments
1.2	10/12/2024	Updated version prepared for back-up dissemination of dust with bias correction added (Figure 4.7) and new cloud mask (see section 4.2.2.4) consistent over the whole IASI time series and between the three IASI instruments, and able to differentiate clouds well from dust plumes. Non reviewed yet.

TABLE OF CONTENTS

**1. INTRODUCTION .....4**

1.1 Objective ..... 4

1.2 IASI instrument..... 4

1.3 Product characteristics overview and context ..... 4

**2. PREFACE .....5**

2.1 Retrieving aerosol in the infrared..... 5

2.2 Detection and aerosol type differentiation ..... 5

2.3 Retrieval and its challenges..... 5

**3. INPUT AND AUXILIARY DATA.....8**

3.1 Forward model parameters..... 8

3.1.1 Surface Parameters..... 8

3.1.2 Aerosol optical and physical properties ..... 8

3.1.3 Altitude ..... 11

**4. ALGORITHM .....13**

4.1 Aerosol detection ..... 13

4.2 Retrieval algorithm..... 19

4.2.1 Data Training set..... 19

4.2.2 Setup and training of the neural network ..... 20

4.2.3 Example ..... 24

4.2.4 Uncertainty characterisation ..... 26

4.2.5 Post-processing ..... 27

**5. REFERENCES .....28**

## 1. INTRODUCTION

### 1.1 Objective

This document describes the dust retrieval algorithm (level 2) for IASI onboard Metop-A, B, and C, developed at ULB (Clarisse et al., 2019) and for which an implementation at EUMETSAT has been agreed in the frame of the AC SAF CDOP-4 project.

### 1.2 IASI instrument

IASI is an infrared Fourier transform spectrometer developed jointly by CNES (the French space agency) with support of the scientific community (for a review see Hilton et al. (2011)), and by EUMETSAT. IASI is mounted on-board the European polar-orbiting Metop satellite with the primary objective to improve numerical weather predictions, by measuring tropospheric temperature and humidity with high horizontal resolution and sampling, with 1 km vertical resolution, and with respectively 1 K and 10% accuracy (Camy-Peyret and Eyre, 1998). As a second priority IASI contributes to atmospheric composition measurements for climate and chemistry applications (Clerboux et al., 2009). To reach these two objectives, IASI measures the infrared radiation of the Earth's surface and of the atmosphere between 645 and 2760  $\text{cm}^{-1}$  at nadir and along a 2200 km swath perpendicular to the satellite track. A total of 120 views are collected over the swath, divided as 30 arrays of 4 individual Field-of-views (FOVs) varying in size from  $36 \times \pi \text{ km}^2$  at nadir (circular 12 km diameter pixel) to  $10 \times 20 \times \pi \text{ km}^2$  at the larger viewing angle (ellipse-shaped FOV at the end of the swath). IASI offers in this standard observing mode global coverage twice daily, with overpass times at around 9:30 and 21:30 mean local solar time. The very good spatial and temporal sampling of IASI is complemented by fairly high spectral and radiometric performances: the calibrated level 1C radiances are at 0.5  $\text{cm}^{-1}$  apodized spectral resolution (the instrument achieves a 2 cm optical path difference), with an apodized noise that ranges below 2500  $\text{cm}^{-1}$  between 0.1 and 0.2 K of a reference blackbody at 280 K (Hilton et al., 2011).

### 1.3 Product characteristics overview and context

The algorithm is based on (1) a sensitive hyperspectral dust index and (2) the conversion of the index to optical depth at 10  $\mu\text{m}$ . The dust index is derived from a Jacobian, encompassing a typical infrared dust signature and a covariance matrix, derived from spectra without observable quantities of dust. The conversion to optical depths (ODs) relies on a neural network (NN), trained from a database of synthetic spectra, a CALIPSO dust climatology and IASI L2 meteorological data (pressure, temperature, humidity profiles). This document gives a detailed description of all these different aspects, and of the specific assumptions and known limitations of the IASI dust algorithm.

## 2. PREFACE

### 2.1 Retrieving aerosol in the infrared

Infrared sounders have historically mainly been used for (ice)cloud detection and retrieval, even though it was recognised early on that the atmospheric window  $750\text{-}1250\text{ cm}^{-1}$  region is also sensitive to mineral aerosol (windblown dust and volcanic ash). This is mainly the case because of the strong Si-O resonance band situated around  $1000\text{ cm}^{-1}$  (Hoidale & Blanco, 1969; Volz, 1973; Toon et al., 1977; Hunt, 1982). Infrared sounders offer complementary measurements of aerosols to UV/Vis sounders, being able to measure in the absence of solar radiation (at night) and with enhanced sensitivity to the coarse mode. High-resolution sounders in addition offer sensitivity to aerosol size; altitude and composition (see next section). In this chapter, we give a brief overview of published retrieval approaches of airborne minerals from hyperspectral infrared sounders.

### 2.2 Detection and aerosol type differentiation

Retrieval of aerosol properties in the infrared is often preceded by a detection and/or differentiation phase, where observations are flagged for the presence of a certain type of aerosol. This has two advantages; firstly, this avoids (often computationally expensive) full retrievals of observations without detectable quantities of aerosol. Secondly, the retrieval itself can often be simplified if the presence of one specific type of aerosol can be assumed. Current high resolution infrared sounders such as AIRS or IASI are able to detect and differentiate a range of different aerosol types, such as volcanic ash, windblown dust, smoke, sulphuric acid droplets, ammonium sulphate as was shown in Clarisse et al. (2013). This study also presents an overview of the typical methods that are applied for detecting aerosol in the infrared. Here we list the main approaches. Example references are also given, where possible related to detection of mineral aerosol from hyperspectral sounders.

- A. Feature detection. Typically, these methods work by setting thresholds on brightness temperature differences (BTD) (e.g. (DeSouza-Machado et al. 2006; Vandenbussche et al. 2013)). This is the simplest, but perhaps also the most transparent detection method.
- B. Distance measures, here the observed spectra are matched to spectra contained in look up tables and then classified based on the results (e.g. (Clarisse et al., 2010a)).
- C. Singular value decomposition and principal component analysis. These approaches have the inherent advantage of relying on a large ensemble of (observed) spectra and exploiting a large spectral range (e.g. (Hurley et al., 2009; Klüser et al., 2011)).
- D. Retrieval or pseudo-retrieval approaches. Here fitting techniques are directly used, either as a first estimate of the quantity (and thus detection) or to circumvent the detection altogether.

The unified aerosol detection technique, which was presented in Clarisse et al. (2013), combines ideas from B, C and D, and is the one used here. It will be summarized in section 4.

### 2.3 Retrieval and its challenges

At the core of almost all aerosol retrieval algorithms is a forward model that can model the outgoing longwave radiation given suitable input parameters on the state of the surface and atmosphere. For aerosols, it is important to take into account the effects of multiple scattering. The inverse model or retrieval attempts to retrieve atmospheric (aerosol) properties from an observed spectrum. For aerosols, the most common types of inverse models are those relying on spectral fitting, where the

observed spectrum is iteratively matched with the simulated spectrum. The advantage of this approach is that the background atmosphere can be fully taken into account; however, a major disadvantage is its computational cost. Algorithms based on lookuptables (LUTs) are typically at least an order of magnitude faster. These lookuptables contain precalculated spectra generated from a set of different atmospheric/surface input parameters. The challenge for this approach is to make the LUT representative enough for the range of observable spectra.

Whether a retrieval approach is based on spectral fitting or LUTs, there are a number of key parameters that need to be taken into account:

1. *The source function (surface temperature and surface emissivity)*

The source function determines how much radiation is emitted from the Earth and how much will reach the aerosol layer. It is a vital parameter for the determination of an accurate OD. The importance of surface emissivity cannot be underestimated as in the infrared it is dependent on the wavenumber. Surface emissivity over ocean can be modelled but over land spectrally, spatially and temporally resolved databases are required.

2. *The aerosol layer temperature (or equivalently altitude)*

This parameter determines how much radiation will be reemitted by the aerosol layer (for a given OD). As the source function, the aerosol layer temperature is one of the most important parameters.

3. *The optical properties (aerosol refractive index, particle shape and size distribution).*

Optical properties of the aerosol under consideration need to be known, so that observed spectra can be accurately simulated with the forward model. The particle shape is usually taken to be spherical for the retrieval of mineral aerosol in the infrared. The size distribution is often assumed lognormal, whereas the effective radius is a parameter which is sometimes included in the retrieval. It is not the most critical parameter for the estimation of the OD though.

4. *The background atmospheric state (trace gas profiles and temperature profiles)*

Water vapour continuum especially can affect the baseline in the atmospheric window drastically, and has to be accounted for in the retrieval. Depending on the choice of wavelength range, also the variability of ozone needs to be considered.

5. *Meteorological clouds*

Either clouds should be taken into account in the retrieval or cloud free scenes have to be determined.

Some of these key parameters can be retrieved simultaneously with the aerosol parameters of interest; others are best obtained from auxiliary (third party) sources. While an accurate retrieval critically hinges on the accurate knowledge of these, limited or uncertain knowledge of any of them can sometimes be circumvented by selecting only a subset of the observed channels in the retrieval, which minimizes the influence of the unknowns, while maximizing the sensitivity to the parameters of interest. A summary of published retrieval methods and some of their characteristics is listed in Table 2.1.

The theoretical basis and practical implementation of the ULB NN algorithm will be outlined in the next sections. Most of the information is taken from Clarisse et al. (2019) where the retrieval algorithm is described in detail. The IASI instrument is described on Section 1.2. The choice of the input parameters/auxiliary data for the algorithm described in this document will be justified and



outlined in Section 3. The retrieval algorithm itself and a comprehensive error characterisation is presented in Section 4. The output data format is presented in Section 5.

**Table 2.1 Overview of published dust retrieval algorithms for IASI/AIRS**

References	Retrieval	Spectral range	Retrieved dust quantities	Atmosphere (temperature and humidity)	Size distribution	Refractive indices	Surface emissivity	Comments
Capelle et al. (2018) and references therein	Multistage look-up table	26 channels	OD, effective radius, altitude	Retrieved	Lognormal ( $\tau_g = 0.79$ , $\sigma = 1.92$ )	OPAC, Hess et al. (1998)	Capelle et al. (2012)	
DeSouza-Machado et al. (2006); and DeSouza-Machado et al. (2010)	Spectral fit	36 channels in 800–1,250 $\text{cm}^{-1}$ and at $\sim 2,600 \text{ cm}^{-1}$	OD	ECMWF, surface temperature retrieved	Lognormal ( $\sigma = 2$ )	Volz (1973)	Masada et al., (1988; ocean) and Seemann et al. (2008; land)	Details refer to the 2010 publication
Yao et al. (2012)	Spectral fit	8 channels in 670–972 $\text{cm}^{-1}$	OD, altitude	ECMWF	From in situ measurements, Han et al. (2012)	OPAC, Hess et al. (1998)	Seemann et al. (2008)	
Vandenbussche et al. (2013)	Spectral fit	900–930 $\text{cm}^{-1}$ and 1,095–1,125 $\text{cm}^{-1}$	OD, vertical profile	ECMWF/IASI L2	Lognormal ( $\tau_g = 0.5$ , $\sigma = 2.2$ )	Volz (1972b)	Zhou et al., (2011; land) and Newman et al. (2005; ocean)	
Klüser et al., (2011, 2012)	Singular value decomposition	20 channels in 830–1,250 $\text{cm}^{-1}$	OD (altitude)	Not used	Lognormal (multiple from OPAC)	OPAC, Hess et al. (1998) and various minerals	Not used	
Cuesta et al. (2015)	Spectral fit	11 microwindows in 831–1,183 $\text{cm}^{-1}$	OD, vertical profile	ECMWF and retrieved	Lognormal ( $\tau_g = 0.92$ , $\sigma = 1.75$ )	OPAC, Hess et al. (1998)	Zhou et al. (2011)	
Ventress et al. (2016)	Spectral fit with a generalized error covariance matrix	680–1,200 $\text{cm}^{-1}$	OD, altitude, and effective radius	ECMWF	Lognormal ( $\sigma = 2.0$ )	Eyjafallajökull indices		Volcanic ash only
Charisse et al. (2010) and Newman et al. (2012)	Spectral fit	750–1,250 $\text{cm}^{-1}$ or subrange	OD, effective radius	IASI L2	Lognormal ( $\tau_g = 0.5$ , $\sigma = 2.0$ )	Volz (1973), Balkanski et al. (2007)	Constant	Also applied to other aerosol types
Moxnes et al. (2014)	Look-up table	100 channels in 750–1,250 $\text{cm}^{-1}$	OD, altitude, effective radius	IASI L2	Lognormal ( $\sigma = 2.0$ )	Pollack et al. (1973) and Eyjafallajökull indices	Constant	Volcanic ash only
Present study	Neutral network	100 channels in 750–1,250 $\text{cm}^{-1}$	OD	IASI L2	Lognormal ( $\tau_g = 0.5$ , $\sigma = 2.0$ )	Volz (1973)	Zhou et al., (2013; land) and Nalli et al. (2008; ocean)	

Note. AIRS = Atmospheric Infrared Sounder; IASI = Infrared Atmospheric Sounding Interferometer; ECMWF = European Centre for Medium-Range Weather Forecasts; OD = optical depth; OPAC = Optical Properties of Aerosols and Clouds.

## 3. INPUT AND AUXILIARY DATA

### 3.1 Forward model parameters

#### 3.1.1 Surface Parameters

##### 3.1.1.1 Surface elevation

The first important parameter is the surface elevation, which was here taken from the “National Geophysical Data Center TerrainBase Global DTM Version 1.0” and downloaded from [ftp://ftp.ngdc.noaa.gov/Solid\\_Earth/cdroms/TerrainBase\\_94/](ftp://ftp.ngdc.noaa.gov/Solid_Earth/cdroms/TerrainBase_94/). The used file is tbase.bin. This data is also used for land/sea flagging. This data has a resolution of 05' 00" for both latitude and longitude.

##### 3.1.1.2 Surface emissivity

For modelling water surface emissivity, very reliable models exist. Here we used the data from Nalli et al. (2008) currently used in Community Radiative Transfer Model (CRTM) (data provided by Paul van Delst, private communication). This emissivity data is dependent on the wavenumber, the viewing angle and the wind surface speed. Because the latter is unknown, we used an average value of 6m/s everywhere.

Land emissivity is more difficult to model, but there are now several datasets available that were derived from IASI. Here the monthly climatology from Zhou et al. (2011) and Zhou et al. (2013) is used. Although every effort has been made to remove the influence of aerosols and clouds on this product, residual contamination by e.g. dust aerosols in some areas cannot be excluded.

#### 3.1.2 Aerosol optical and physical properties

##### 3.1.2.1 Size distribution

Aerosols are commonly characterised by a (multimode) lognormal size distribution. This distribution is defined as  $N(r) = \frac{N_0}{\sqrt{2\pi} \ln(\sigma_g) r} \exp\left(-\frac{\ln^2(r/r_g)}{2 \ln^2(\sigma_g)}\right)$ , with  $N_0 = \int_0^\infty N(r) dr$  the total number of particles. Here  $r_g$  and  $\sigma_g$  are called the geometric mean radius and geometric standard deviation respectively. For OD retrievals from infrared observations, unlike for mass retrievals, size distributions are not that critical (Pierangelo et al., 2004). The width of the distribution especially will determine the very small and very large particles, for which the longwave infrared measurements are not sensitive. Following other retrieval schemes (see Table 1.1), published aerosols models (Hess et al., 1998) and measurement data (Reid et al., 2003), we have settled on mean values of  $r_g = 0.5$  and  $\sigma_g = 2$ .

### 3.1.2.2 Refractive index

Just like the size distribution, the refractive index is a parameter that needs to be defined for the retrieval. The specific choice of refractive index is however unlikely to influence the retrieval value of the optical depth greatly (Peyridieu et al., 2010).

Since the 1960s only few measurements have been made in the infrared which are representative for transported dust. The situation is fortunately improving, and in the past years, several new measurements have become available. As an alternative to direct measurements, synthetic refractive indices can be used, calculated from applying suitable mixing rules on refractive indices of pure minerals. In Table 3.1 a compilation is presented of most public measured or calculated refractive indices of dust and sand, most data can be found in the databases HITRAN, GEISA and ARIA (Gordon et al., 2020; Delahaye et al., 2021).

**Table 3.1 Public measured or calculated refractive indices of dust and sand.**

<i>Measured and Calculated Refractive Index Data of Dust and Sand in the Thermal Infrared</i>		
Description	Range (cm <sup>-1</sup> )	References and comments
<b>Measurements</b>		
Dust from precipitation (midlatitude rained out mixtures of soil particles, fly ash/soot and pollen)	250–50,000	Volz (1972b), samples described in Volz (1972a), tabulated in D'Almeida et al. (1991); Shettle and Fenn (1979); World Meteorological Organization (1986); and referred to as “dust-like”; termed “insoluble” in Koepke et al. (1997) and Hess et al. (1998)
Midlatitude dust	333–4,000	Volz (1983), two size classes
Saharan dust, Niamey, Niger	250–4,000	Fouquart et al. (1984, 1987)
Saharan sand, Barbados, West Indies	250–4,000	Volz, (1973, figure)
Saharan sand, Mauritania, dry and 50% relative humidity	470–6,980	ARIA (2017) measurements made by D. Peters
Afghanistan, Tadjikistan sand	400–4,000	Sokolik et al., (1993, 1998)
Negev, Israel clean and dust storm	833–1,333	Fischer (1976) (see also Sokolik et al., 1998)
Dust in Southwest United States, Texas	625–1,000	Patterson (1981), imaginary part only; real part calculated and shown in Sokolik et al. (1998)
Niger, Algeria, Tunisia, and the Gobi desert	400–4,000	Di Biagio, Boucher, et al. (2014) and Di Biagio, Formenti, et al. (2014)
9 different global dust source areas (19 samples)	666–3,333	Di Biagio et al. (2017)
<b>Mixtures</b>		
GADS/OPAC mineral component	250–4,000	Koepke et al. (1997) and Hess et al. (1998); Mainly Volz (1973) with addition of extra quartz absorption features
Mixture of hematite and quartz; hematite is 10% by volume	33–50,000	Longtin (1988)
Composite clay (1/3 by weight of montmorillonite, illite, and kaolinite)	50–4,000	Querry (1987)
Composite of hematite, illite, montmorillonite, quartz, kaolinite, and calcite	100–34,722	Balkanski et al. (2007)

*Note.* Most data can be found in the HITRAN (Massie & Hervig, 2013), GEISA (Jacquinet-Husson et al., 2016), and ARIA (ARIA, 2017) spectral databases. OPAC = Optical Properties of Aerosols and Clouds; GADS = Global Aerosol Data Set; HITRAN = HIgh Resolution TRANsmission molecular absorption database; GEISA = Gestion et Etude des Informations Spectroscopiques Atmosphériques.

To decide which refractive index would be used, 41 spectra with a strong dust signature were selected over 10 days in June 2013 over the Atlantic Ocean (IASI-A data). This region was chosen, as it is area in the world where transported dust is most easily observed, and as it is over ocean, it allows us to focus on the refractive index without worrying about potential emissivity problems. An optimal estimation fit of the aerosol content and interfering trace gases is outlined in Clarisse et al. (2010b) for 7 different refractive indices. The average residuals (differences of observed- calculated spectrum) in brightness temperatures are shown in the figure below.

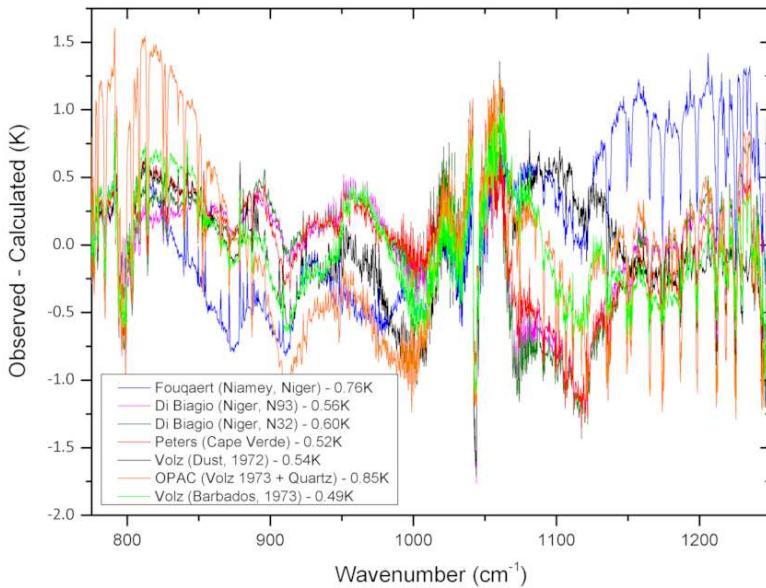


**Figure 3.1:** Retrieval residuals with 7 different refractive indices.

Note that in this figure, the residual around  $1050\text{ cm}^{-1}$  should be disregarded, as no attempt was made to fit the ozone band accurately. The Fouqaert index stands out with a high fit residual, and fails to catch the overall V shape as accurately as the others do. The Volz indices on the other hand provide the best fit, especially the measurement made from Barbados sand. This is not surprising as sand found at that location is perhaps the most representative for long-range transported Saharan dust. Also the Peters measurements from Cape Verde sand perform well. The new Di Biagio measurements provide a reasonably accurate fit, although consistently underestimate the extinction near  $1100\text{ cm}^{-1}$ . The OPAC index, which

was obtained from the Volz index with the addition of quartz features, gives the worst fit of all. The strong quartz feature at  $800\text{ cm}^{-1}$  that is clearly seen in the residual, is not seen that strongly in the observed spectra.

From Figure 3.1 we conclude that either the Volz Barbados or the Peters Cape Verde indices are most suitable. In the end we have decided to use the Volz indices as (1) they provided the best fit, (2) they are readily available, and (3) they are used in many other retrieval schemes, including the ones from project partners. Finally, Figure 3.2 shows the mean observed and calculated spectra from our test case of 41 spectra.

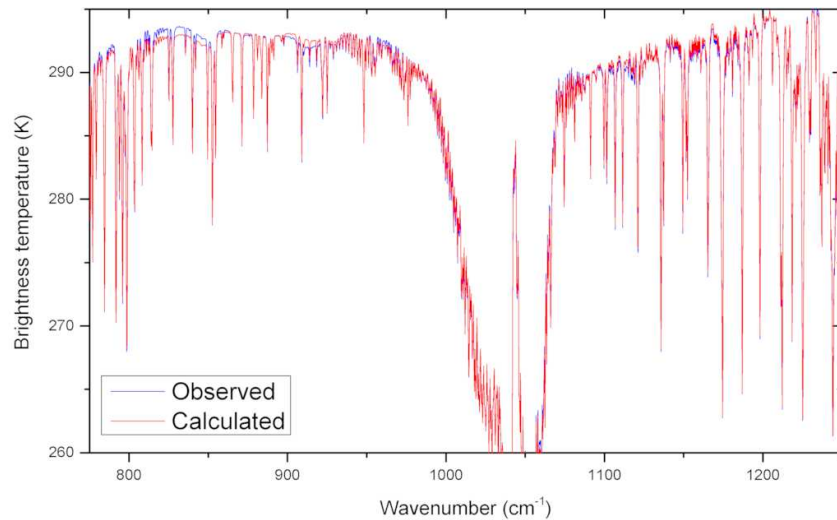


**Figure 3.2:** Mean observed and calculated spectrum with the Volz (1973) refractive indices.

### 3.1.3 Altitude

Aerosol dust altitude can be retrieved in the infrared for large ODs. However, the uncertainties become too large in the general case, so that one has to resort to retrieval schemes which use information from multiple pixels (monthly (Peyridieu et al., 2010) or regional averages using a priori information (Vandenbussche et al., 2013)). For this reason, and for overall consistency and quality control, we have opted here to work with a monthly climatology derived from CALIPSO (Yu et al., 2010) observations (version 4.1).

The approach that we followed is very similar to the one presented in Tsamalis et al. (2013). As input for the climatology the Lidar Level 2 Vertical Feature Mask was used for all CALIOP observations from 2007 to 2013. The CALIOP data were obtained from the NASA Langley Research Center Atmospheric Science Data Center. From this data all layers (which included multi-layered structures) were extracted which were classified as ‘dust’, ‘polluted dust’ or ‘dusty marine’ with a high feature QA and a confident cloud/aerosol assessment. For each such layer the mean altitude (defined as the mean between the top and the bottom of the layer) was stored. To remove noise, only layers below 7 km were considered. Then all data were gridded ( $1^\circ$  by  $1^\circ$ ) and averaged for one-month periods, calculating both the mean and standard deviation. To reduce the apparent noise, grid boxes with fewer than 150 measurements were assigned a standard deviation of 2 and a mean of 3 km. As a result, a  $1^\circ \times 1^\circ$  monthly dust altitude climatology is obtained consisting of a mean altitude (shown in Figure 3.3) and corresponding standard deviation.

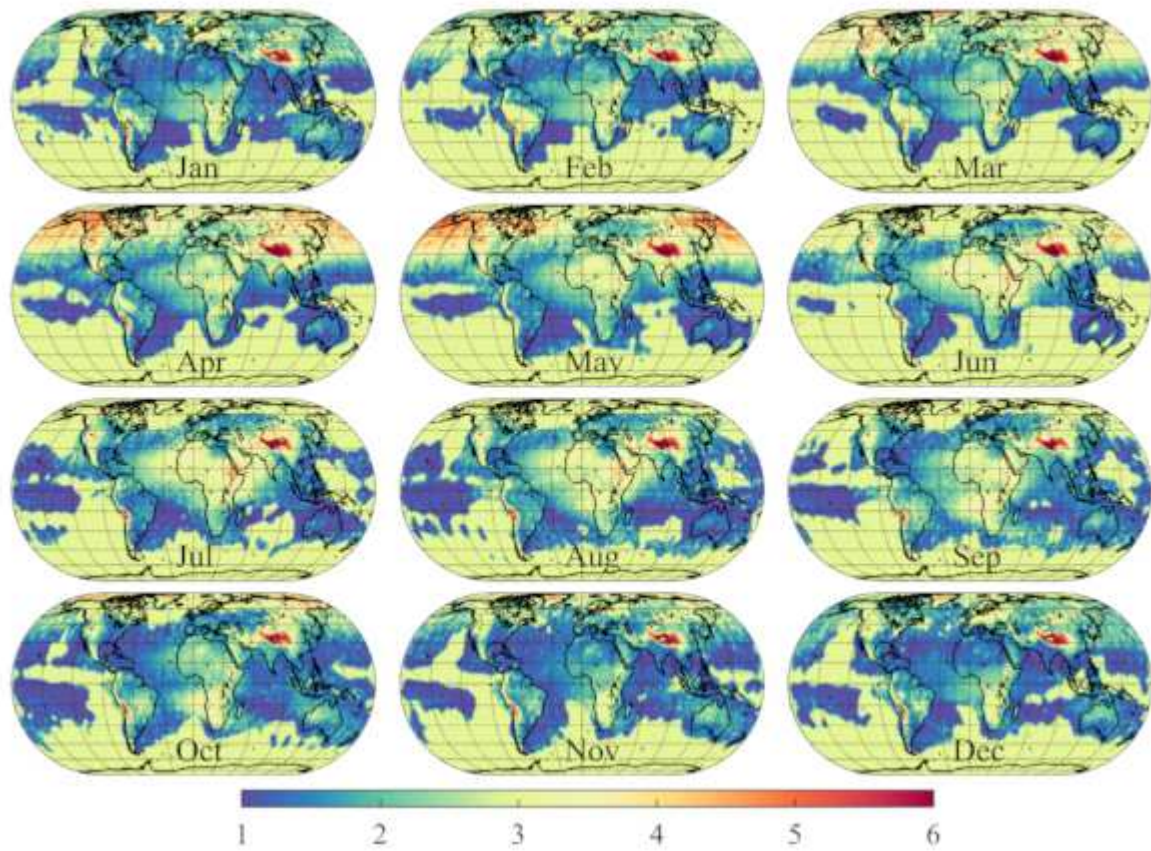


**Figure 3.3:** Dust altitude climatology (in km) derived from Cloud-Aerosol Lidar and Infrared Pathfinder Satellite Observation data.

## 4. ALGORITHM

### 4.1 Aerosol detection

The basis of the dust detection scheme that has been employed here has been discussed in detail in Clarisse et al. (2013 and 2019). A flowchart of the retrieval framework is shown in Figure 4.1. We summarize the method briefly below.

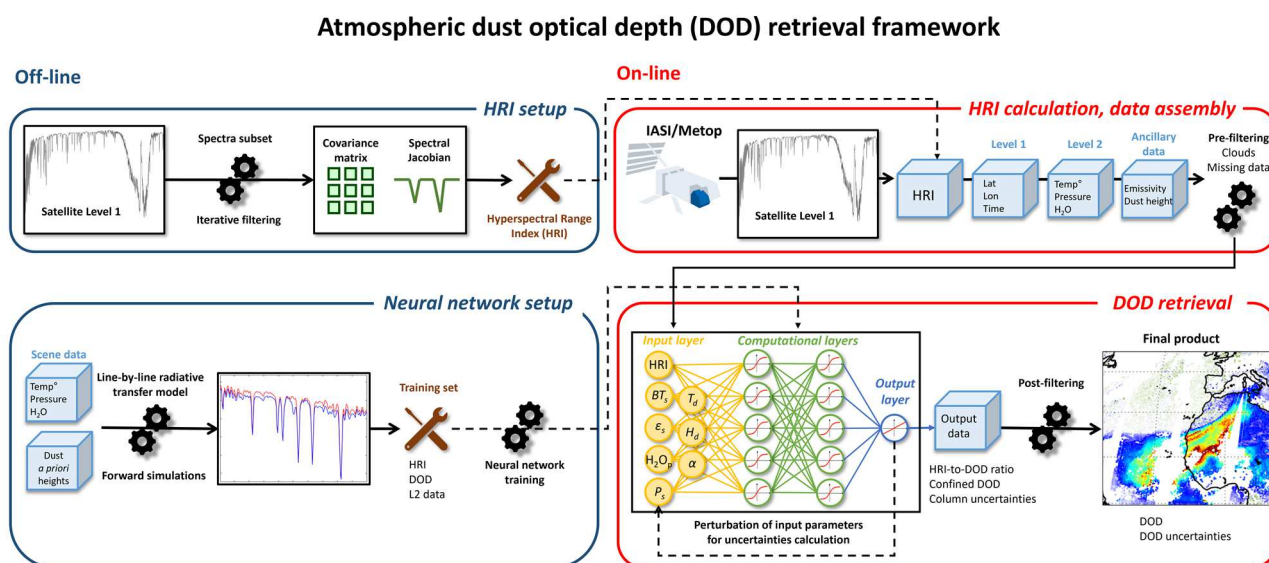


**Figure 4.1:** Flowchart showing the IASI atmospheric dust optical depth retrieval framework.

A crucial feature of the method is that it does not rely on any forward simulations; instead, it uses real observed IASI spectra of aerosol dust as the basis of the detection. In the original method, 11 averaged dust spectra were used. To simplify further processing in the NN, a single Jacobian was sought, for which the detection was satisfactory both over ocean and over land. Therefore, among the many different Jacobians that were generated, one particular one, shown in Figure 4.2, was selected that resulted in a detection that was globally satisfactory and almost equivalent with the approach that used several classes. The Jacobian was calculated from spectra observed over Morocco in June 2013.

As well as information on the spectral signature of dust, we need to capture the spectral information of clear spectra (uncontaminated with dust). For this, we use a global mean  $\mu_c$  and covariance matrix  $S$  of clear spectra both for land and over sea separately (this as explained in Clarisse et al. (2013 and 2019) was trained recursively, as detection gets better, the mean and covariance matrix can be updated).

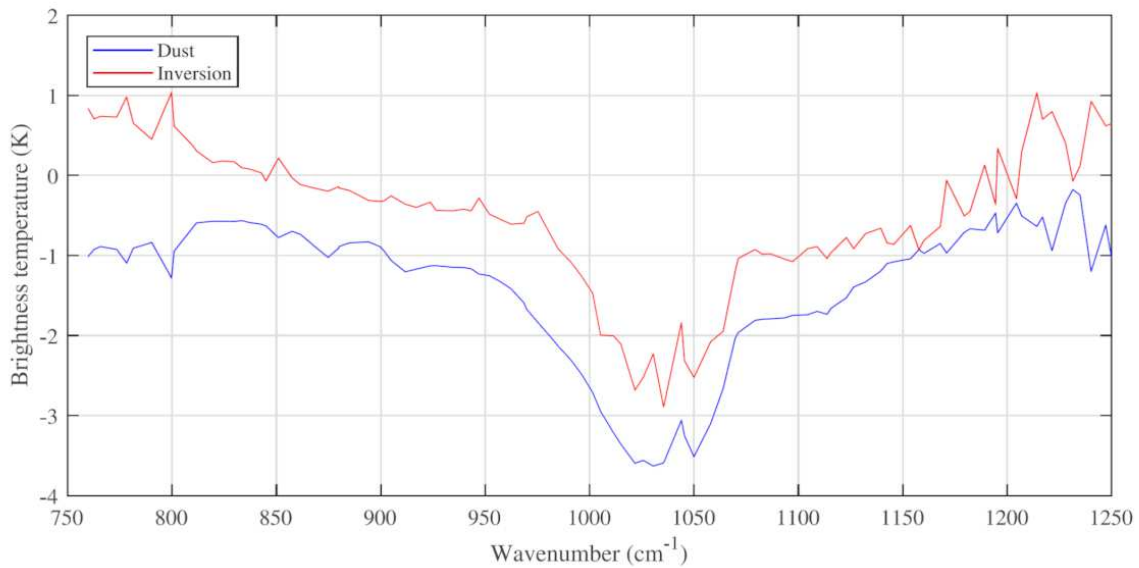


**Figure 4.2:** The IASI-derived Jacobian used for dust detection (blue) together with the Jacobian used for the removal of false detection due to large temperature inversions (red). The spectra shown have a reduced sampling of 100 channels.

The actual detection is based here on linear discrimination analysis (but has also a relation with optimal estimation (Walker et al., 2011)):

$$R(y) = \frac{k^T S^{-1}(y - \mu_c)}{\sqrt{k^T S^{-1}k}}$$

With  $y$  the observed spectrum and  $k = \mu_p - \mu_c$ , where  $\mu_p$  refers to the potential dust-polluted spectra. The quantity  $y$  is normalized so that for clear spectra the mean equals 0 and the standard deviation equals 1. So that 99.7% of clear spectra will have an  $R$  value within  $\pm 3$ . Suitable thresholds on this value can therefore detect dust. This relative distance criterion is very good at detecting dust, but typically suffers from too many false detections due to surface emissivity features over deserts and ice.

To resolve these over desert, a monthly averaged  $R$ -bias was calculated from months where no or not much dust is to be expected as illustrated in Figure 4.3. This bias was then subtracted from each individual observation (based on the closest grid point and only over desert). Figure 4.4 illustrates this bias correction for northern Africa and the Middle East. The top left panel shows the calculated bias. On the top right a visible map is shown. The superimposed contour delineates where the bias changes sign; it is clear that these transitions correspond to changes in surface type (rocky soils typically exhibit a positive bias and sandy soils a negative bias). The bottom panels illustrate the bias correction on May 2013. The bottom left panel shows an uncorrected average of  $R$  values, where despite the change of color scale, some of the features in the top panels can still be recognized. The average of the debiased  $R$  values is shown on the bottom right and is visibly smoother than the left panel.

To resolve the false detections over ice and snow, we decided to exclude observations over ice and snow from the processing chain as no dust observations are expected there anyway. For this a monthly

climatology was built using ERA ECWMF reanalysed data of ice and snow cover, where we disregard observations where there is on average more than 30% sea-ice or 2 cm snow in addition to some manually chosen areas.

Biases over coastal areas due to temperature inversions on warmer seasons are variable and cannot easily be corrected. Because of this, affected observations are filtered out from further processing using a dedicated flag. This flag is setup similarly as the dust detection flag, and an  $R_{inv}$  value is calculated with the inversion Jacobian (see Figure 4.5). Whenever  $R_{inv}$  exceeded a value of 2 and the dust  $R$  value, the observation is considered to be dominated by this inversion effect and is excluded from further processing. The fraction of these on the total number of cloud-free observations is shown in Figure 4.5 for the year 2013 (left panel). The fraction of dust detections over the remaining observations is shown on the right. Dust detection thresholds of 2 and 3 were applied respectively over ocean and land.

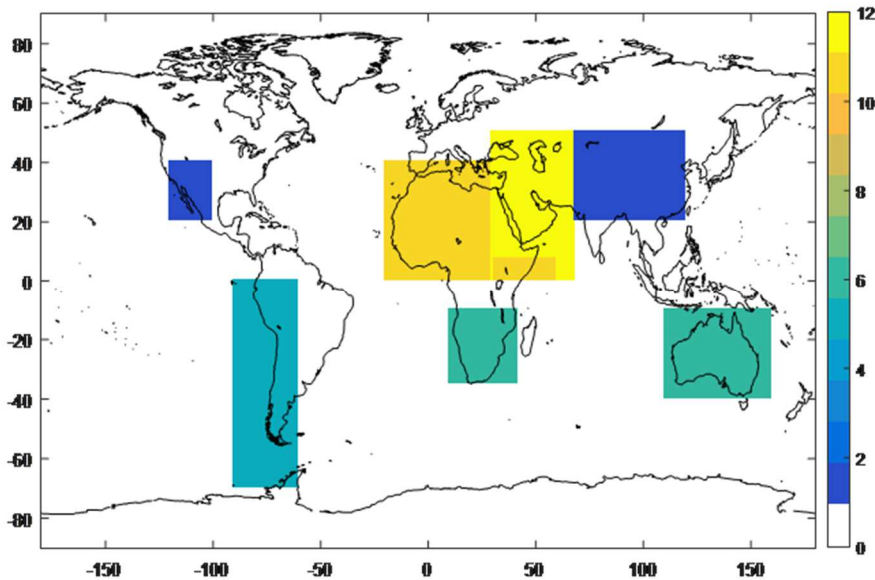


**Figure 4.3:** Month where the lowest dust AOD is expected over deserts. The color scale shows the months from January (1) to December (12).

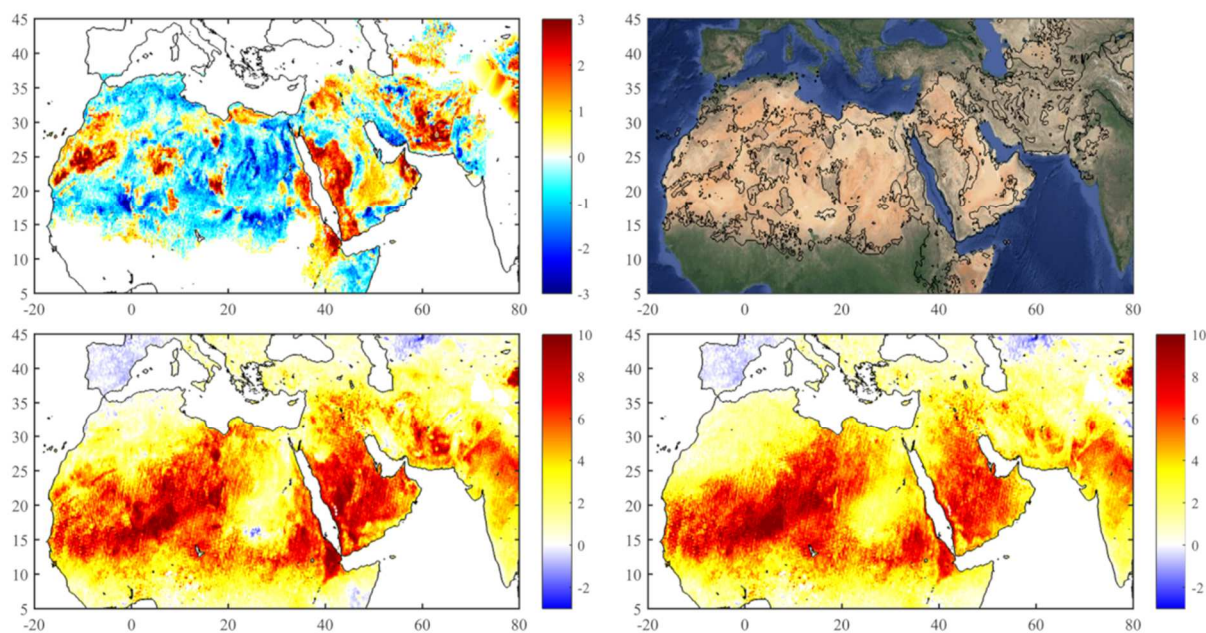


**Figure 4.4:** Bias correction of the dust index  $R$  over deserts. The top left panel shows the observed bias over the (area-dependent) months where little or no detectable dust is expected. The top right panel is a visible map; the superimposed black line delineates the sign changes in the bias (thus corresponding to the transition from yellow to blue in the first panel). The bottom panels show respectively the uncorrected (left) and corrected (right) gridded May 2013 average of the  $R$  value (unitless) over land.

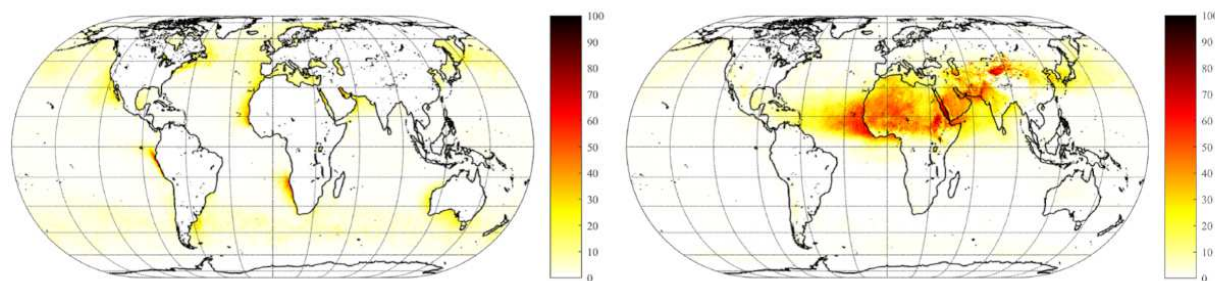


**Figure 4.5:** Percentage of cloud-free daytime observations in 2013 that are removed as they are potentially affected by temperature inversions (left panel), and the percentage of remaining observations detected as dust (right panel).

Since version 9 of the Dust Product, two additional bias corrections are also included. These biases were revealed by the analysis of the time series of the daily mean  $R$  values over remote areas (with no dust contamination) as illustrated in Figure 4.7 (top panel) for one large region above the Indian Ocean (region 3, Figure 4.6). The first one is a systematic shift in the  $R$  values between Metop-B and Metop-A before August 2017. A similar shift, but lower in magnitude, is also observed between Metop-C and Metop-A. For Metop-B, the agreement with Metop-A becomes much better after the 01 August 2017 following an update in the IASI Level 1C radiance spectra (change of the non-linearity coefficients of Metop-B). To correct for the offset with Metop-A, a constant  $R$ -bias evaluated from the observations of three dust-free regions (see Figure 4.6) is simply subtracted from each individual  $R$  values from Metop-B (prior to the 01 August 2017) and Metop-C observations. The times series of the  $R$  after the correction is shown on Figure 4.7 (middle panel).

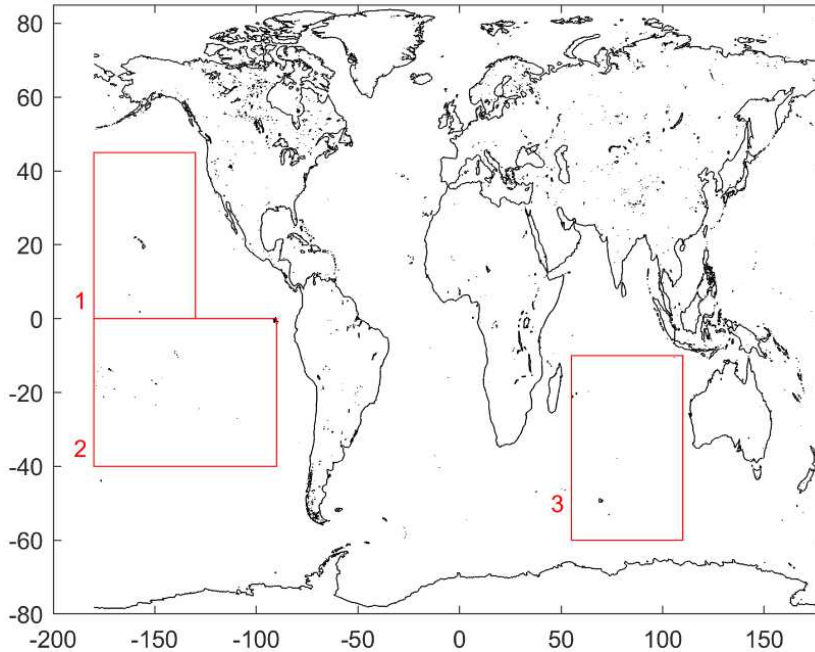


**Figure 4.6:** Dust-free regions (1: Northern Pacific, 2: Southern Pacific, 3: Indian Ocean) considered for the calculation of the offset and the trend bias correction.

The second bias is a clear negative trend in the mean R values, likely due to the changes in the atmospheric concentrations of long-lived species (mainly CO<sub>2</sub> and to a lesser extent CH<sub>4</sub> and N<sub>2</sub>O) which influence some of the channels considered for the calculation of R. The correction for the trend is performed by calculating the slope of the linear regression of the daily mean R value between 2007 and 2021 derived from Metop-A data over the three dust-free regions shown on Figure 4.6. The three slopes are then averaged to derive a mean trend correction factor which is applied to each individual observation (Figure 4.7, bottom panel). Since the Jacobian and the covariance matrix used in the calculation of R are derived from 2013 observations, 2013 is considered as the reference year with no correction applied on the first of July 2013. Before and after, the corrected R ( $\tilde{R}$ ) is simply obtained by subtracting to the initial R value the product of the slope (m) of the linear regression by the number of days since/before 2013/07/01:

$$\tilde{R} = R - m \cdot \Delta t$$

Note that the slope of the linear regression of the daily R values derived from Metop-B observations has also been calculated. As it is very close to the one from Metop-A observations, the choice is made to use the same correction factor derived from Metop-A for the three instruments. The value of the offset and the trend correction is given in Table 4.1.

**Table 4.1** Bias correction parameters

Parameter	Instrument	Value	Date
<b>Bias</b>	Metop-B	0.40	Before 2017/08/01
	Metop-C	0.16	Since launch
<b>Trend</b>	Metop-A, -B, -C	-2.0246 x 10 <sup>-4</sup> /day	Relative to 2013/07/01

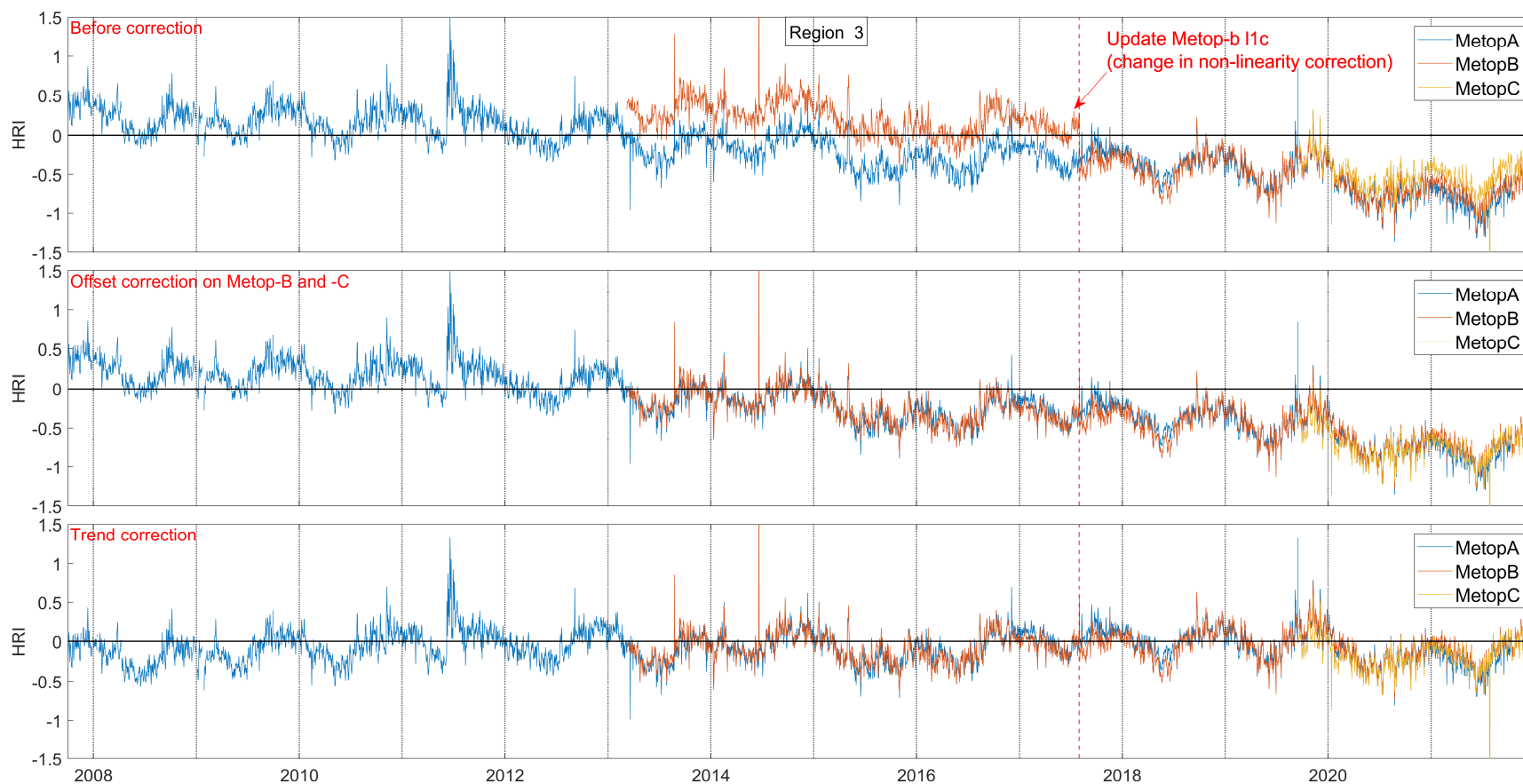


**Figure 4.7:** Example of the time series of R values for Metop-A, -B and -C for one region in the Indian Ocean (region 3 on Figure 4.6), (top) before the biases correction, (middle) after correction for the offset on Metop-B and Metop-C and (bottom) after correction for the trend bias.

## 4.2 Retrieval algorithm

The actual OD retrieval algorithm relies on a NN. The main motivations for this approach are:

1. A multilayer perceptron with one hidden layer can approximate any continuous bounded function arbitrarily closely. While continuity is not automatically guaranteed in our case (for instance when the retrieval problem is under-constrained), for our problem we will show that they can accurately map the retrieval problem.
2. Spectral fitting approaches perform the same expensive calculations (with slightly different input parameters). It can be argued that most of these calculations must be redundant.
3. A NN allows for easy estimating of the propagation of the uncertainties of the input parameters on the network output (the retrieval result).

Any NN needs to be trained with a suitable set of training data, which is discussed in the next section. Note that for the remainder of this section OD refers to the OD at 10  $\mu\text{m}$ .

### 4.2.1 Data Training set

To have maximum control over the training data, it was constructed here from forward simulations using the forward model presented in Clarisse et al. (2010b). The radiative transfer in the forward model uses a four stream adding-doubling approach to deal with the effects of multiple scattering. The aerosol optical properties were calculated with Mie theory from the aerosol properties (refractive index, size distribution) outlined in the previous section.

To make the dataset as representative as possible for actual observed dust spectra, the input parameters (background atmosphere, viewing angle, surface height, emissivity parameters, etc.) for the forward simulation were taken from the auxiliary parameters of the NN-ready files L1C and L2 data (but of course not the observed spectrum). In particular:

- For the year 2013, about 1 in 200 observations were selected with 0% of cloud coverage and to have valid (not non-numeric = NaN) L2 data.
- These observations were further selected so that in 90% dust was detected.

The location of the corresponding scenes that were selected in this way are shown in Figure 4.8.

A random aerosol altitude (between 0.5 and 6.5 km) was assigned to each of the observations. The CALIOP altitude is at this stage not used to make the simulations representative for a larger range of different altitudes. For each of these observations, 10 forward simulations were carried out with varying random OD (between 0 and 3, but with a higher probability assigned to the lower ODs).

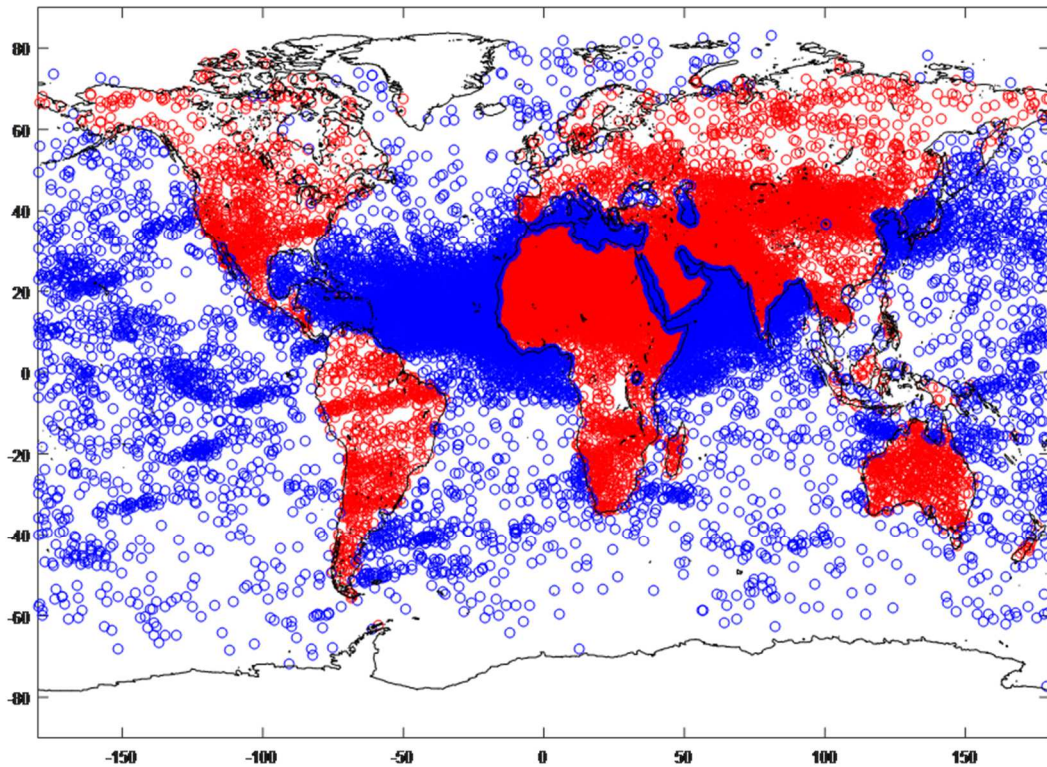


**Figure 4.8:** Location of the atmospheres used for building the training data set (land observations are in red, ocean in blue).

## 4.2.2 Setup and training of the neural network

### 4.2.2.1 Input parameters

The input parameters of a NN should be extensive enough to make the problem well defined, but at the same time, redundancy should be avoided. We first discuss the input parameters related to the spectrum itself and to the surface temperature.

#### 4.2.2.1.1 The V-shape and the R function

In the research phase of this project, first all available spectral channels were used as input. However, we found that although it was very easy to train the network satisfactorily, the network itself was too sensitive to the particular refractive index that was used in the forward simulations. In this case, it appeared that the output was very sensitive to the small-scale features between different spectral channels, rather than the large scale ‘V’-shaped mineral extinction feature. This is a common problem in neural networks, and the solution is often to reduce the number of input parameters. In order to capture the overall extinction feature, a good parameter is the R function, defined in section 4.1. For increasing OD, the R-value increases monotonically (up to saturation levels) as is illustrated in the figure below. Another appealing characteristic of the function is that for constant atmospheric

parameters it is almost linearly related to small ODs. The slope is mainly determined by the thermal contrast that is the temperature difference between the (effective) skin temperature and the atmospheric temperature, which in turns is determined by the aerosol height.

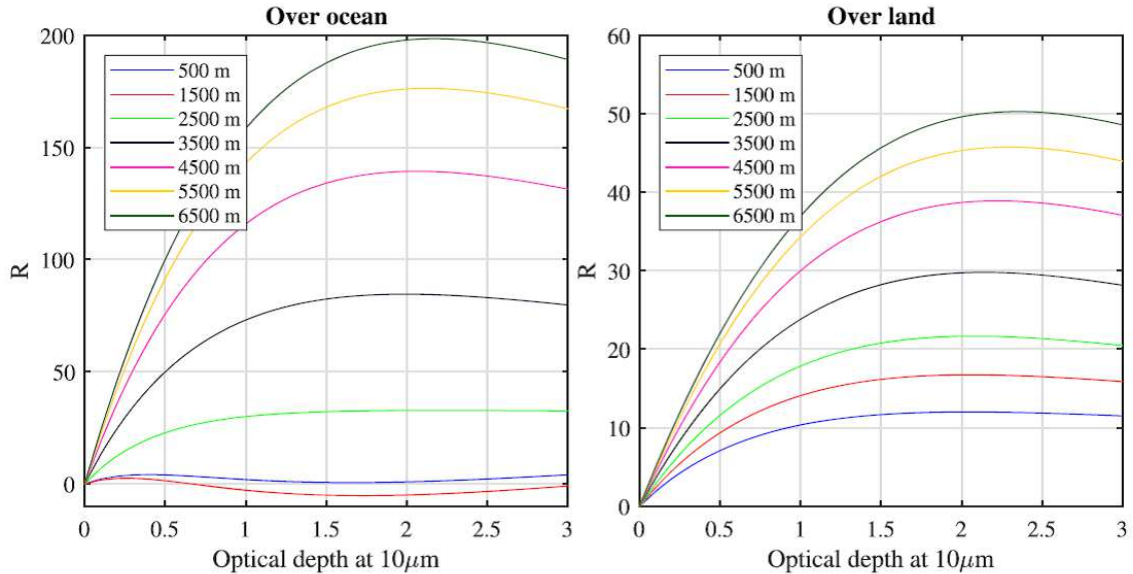


**Figure 4.9:** Dependence of the  $R$  value on altitude and dust OD for (left) an ocean and (right) a land scene.

#### 4.2.2.1.2 The surface temperature

Another input parameter that caused trouble in the initial testing phase was the surface temperature, which as mentioned before is essential for determining the thermal contrast, and hence the  $R/OD$  slope. Unfortunately, even for an advanced hyperspectral infrared sounder as IASI, it can be challenging to retrieve an accurate surface temperature, especially over deserts and in the presence of aerosols. Indeed, the presence of aerosols almost makes it impossible to retrieve surface temperature independently from the aerosol content. To address this issue, rather than using the L2 surface temperature, we added an extra input parameter, set to the mean of the brightness temperature over two selected window channels outside the main ‘V’ feature. This then gives the NN sufficient information on the baseline to work with. Effectively, rather than training the NN to retrieve OD from  $R$  given specified L2 info (including the surface temperature), the NN is then asked to retrieve both the OD and implicitly the surface temperature given  $R$  and the temperature of the baseline.

#### 4.2.2.1.3 Summary of the input data

Below we tabulate the input parameters of the NN. Care has been taken that all major variables are present that affect the observed spectrum, although for instance not all L2 parameters used in the forward simulations have been included, to avoid problems with overfitting. In addition, emissivity parameters have been omitted for observations over ocean, as these are a strict function of the zenith angle.

**Table 4.2** Input data of the neural network

Category	Name
<b>Auxiliary data</b>	Zenith angle (degrees)
	Dust layer height above sea level (km)
	Temperature of the dust layer (K)
	Mean surface emissivity (unitless)
<b>Radiance data (L1C)</b>	Sum of the brightness temperature for the channels at 801 and 809.75 $\text{cm}^{-1}$ (K)
	Dust R values (unitless)
<b>Atmospheric profiles (L2)</b>	Surface pressure (hPa)
	Humidity profiles (5 levels, in partial columns, $\text{molec}/\text{cm}^2$ )

#### 4.2.2.2 Neural network setup

The network itself is a feed-forward network with 12 inputs and 1 output (defined above), two hidden layers with five nodes each and one output layer. The transfer function for the hidden layers is tanh, while the linear transfer function is used for the output layer. Separate networks were setup for ocean and land, as their  $R$  values depend on different covariance matrices.

Levenberg-Marquart was used as the training function with the ‘mean square error’ as performance function. The dataset was divided in 90% train data, 9.9% test data and 0.1% validation data. The test data is used to avoid overfitting, while the validation data is used to evaluate the overall performance of the network on an independent data set.

Rather than using as output the OD, it was found better to use the ratio OD/ $R$  as output parameter. OD’s have a large dynamic range and using those as an output would imply that the absolute error performance function would weigh the errors on the higher ODs relatively higher than the low ODs (and hence would result in poor performance of the network for the higher ODs). On the other hand, a performance function based on the relative error would give too much importance to the very low OD values. For a fixed atmospheric setup, the ratio OD/ $R$  is constant for low values of ODs, and has in any case a small dynamic range, which circumvents the aforementioned problems.

#### 4.2.2.3 Neural network training

Network training takes, depending on the run, about 50-100 iterations, where the performance on the test data is in most cases just slightly below the performance on the training set. This indicates that the network weights are not overly sensitive to the training data.

The training performance is summarized in Figure 4.10 in terms of mean relative errors and biases on the OD, and as a function of OD and altitude. For the calculation of the OD via  $OD = R \times CR$ ,  $R$  was assumed to be noise-free. The relative errors are calculated as the mean of the absolute value of the relative errors for all the observations in a given altitude-OD bin. They are of the order of 10%, except at the lowest altitudes, where they reach 25%. The biases are calculated as the mean of the relative errors. They are mostly close to 0, with a few exceptions again for low altitude. In practice, the uncertainties on all input parameters will lead to larger uncertainties in the retrieved dust OD than the training performance suggests.

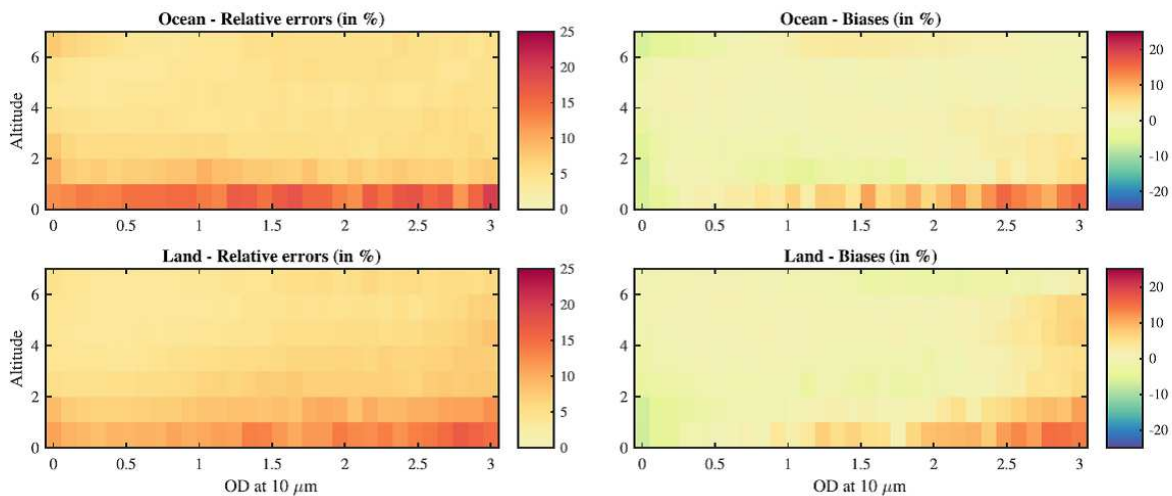


**Figure 4.10:** Performance of the NN on the training data set, in terms of relative errors (left panels) and biases (right panels) (colorscale shows percentage of relative errors/biases) as a function of OD (OD = optical depth) and altitude for ocean (top panels) and land (bottom panels) observations.

#### 4.2.2.4 Pre-filtering

Prior to running the network, the observations undergo a prefiltering operation that selects all spectra for which the retrieval should be performed. This flag determines whether an OD will be retrieved for each observation. It is set if:

- Snow/ice mask is off
- Cloud coverage  $\leq 10\%$
- IASI L2 is available

Since the version 9 of the Dust Product, it was decided to use an alternative cloud product to the operational IASI Level 2 product for the identification of the cloud-free scenes. Indeed, the latter is known to suffer from different issues especially from (1) some discontinuities in the current data record due to different versions of the operational Level 2 cloud product used simultaneously and (2) false cloud detections in the center of large dust plumes (at least for the earlier versions of the cloud product). In version 9, the discrimination between cloud and clear scenes relies on a cloud detection algorithm developed recently by Whitburn et al. (2022). It is based on a supervised neural network (NN) and uses the most recent version (v6.5) of the IASI Level 2 as a reference dataset. The NN product has been demonstrated to be both sensitive to cloud detection and consistent over the whole

IASI time series and between the different instruments on board Metop-A, -B and -C. It is also able to differentiate clouds well from dust plumes.

### 4.2.3 Example

Retrievals for 15 June 2015 are shown in Figure 4.11 for the morning (top) and evening (bottom) overpass. Gaps in the coverage are mostly due to clouds but also due to the other prefilters (see section 4.2.2.4) and postfilters (see section 4.2.4.2). Enhancements are observed where they are expected, that is, over land: Middle East, North Africa, parts of Europe, and central and south Asia, and over ocean: the North Atlantic Ocean, the Caribbean Sea, the Mediterranean Sea, the Red Sea, the Arabian Sea, and Indian Ocean. Especially noticeable is the large dust plume over North West Africa and the North Atlantic Ocean, which is fairly consistent across land-ocean and morning-evening overpass. Over remote regions, the OD values are close to and centered around 0 but are noticeably less noisy over ocean than over land, a direct consequence of the fact that detection is easier over ocean due to the more uniform surface emissivity. Certain land areas also exhibit small local biases (e.g., southeastern part of Africa).

The estimated total uncertainties for 15 June 2015 are shown in Figure 4.12, both as a global distribution and as histogram. In the presence of detectable dust, uncertainties are of the order of 15–30%. Elsewhere, the majority of the uncertainties are in absolute value in the 0.01–0.02 range over ocean and 0.04–0.06 over land. The uncertainties over land during the morning overpass are noticeably smaller due to the better thermal contrast. Finally, note that over some land areas (e.g., South America), some scan angle dependence could be observed for dust ODs close to 0. The reason for this is not clear and it is also not easily corrected for, as it seems present in the dust index itself. Fortunately, such a dependence is not seen in the areas most affected by dust.

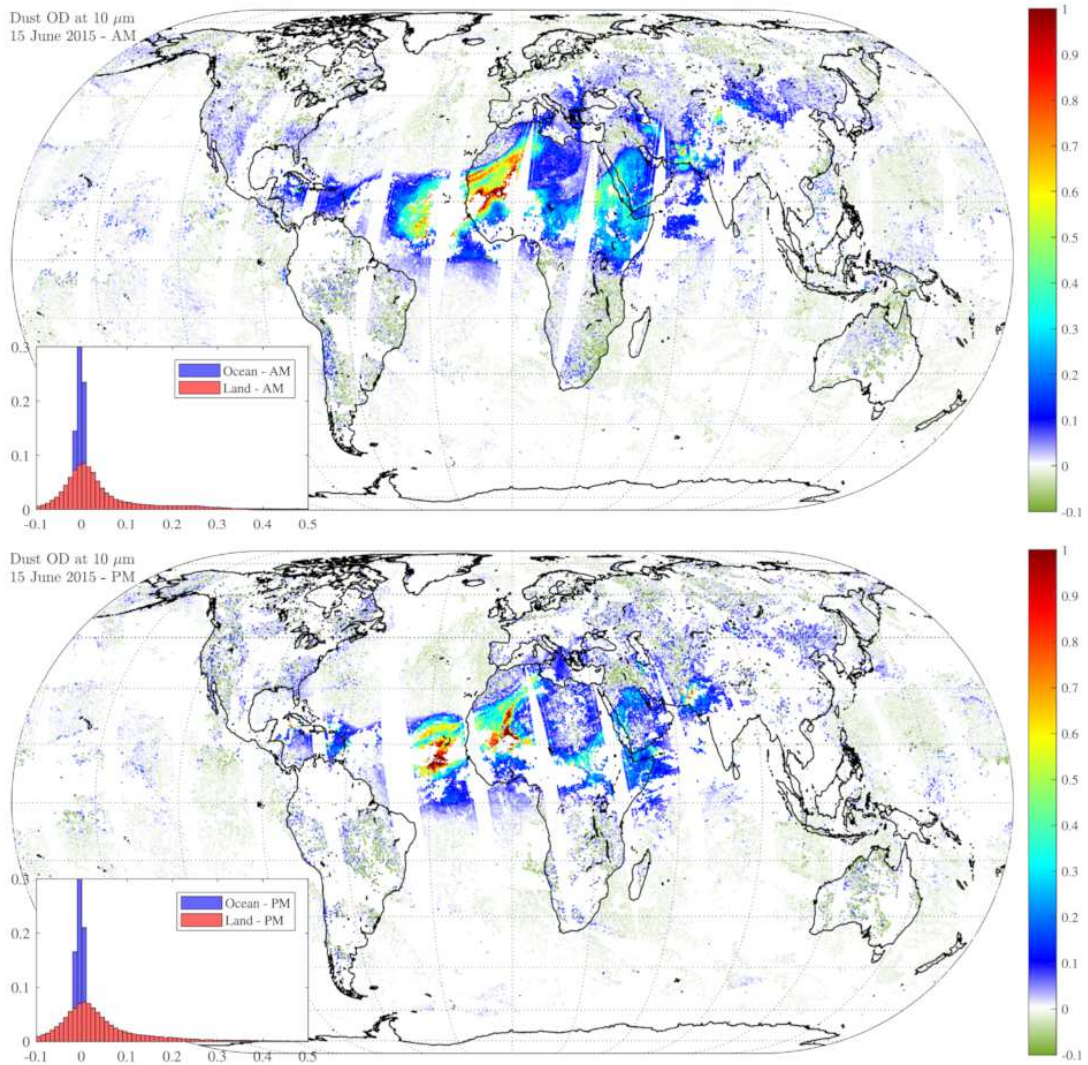


**Figure 4.11:** IASI-retrieved dust OD at 10µm (unitless) for 15 June 2015 for the morning (top) and evening (bottom) overpass. The insets show the probability histograms (frequency of each OD value) of the retrieved values over the entire globe.

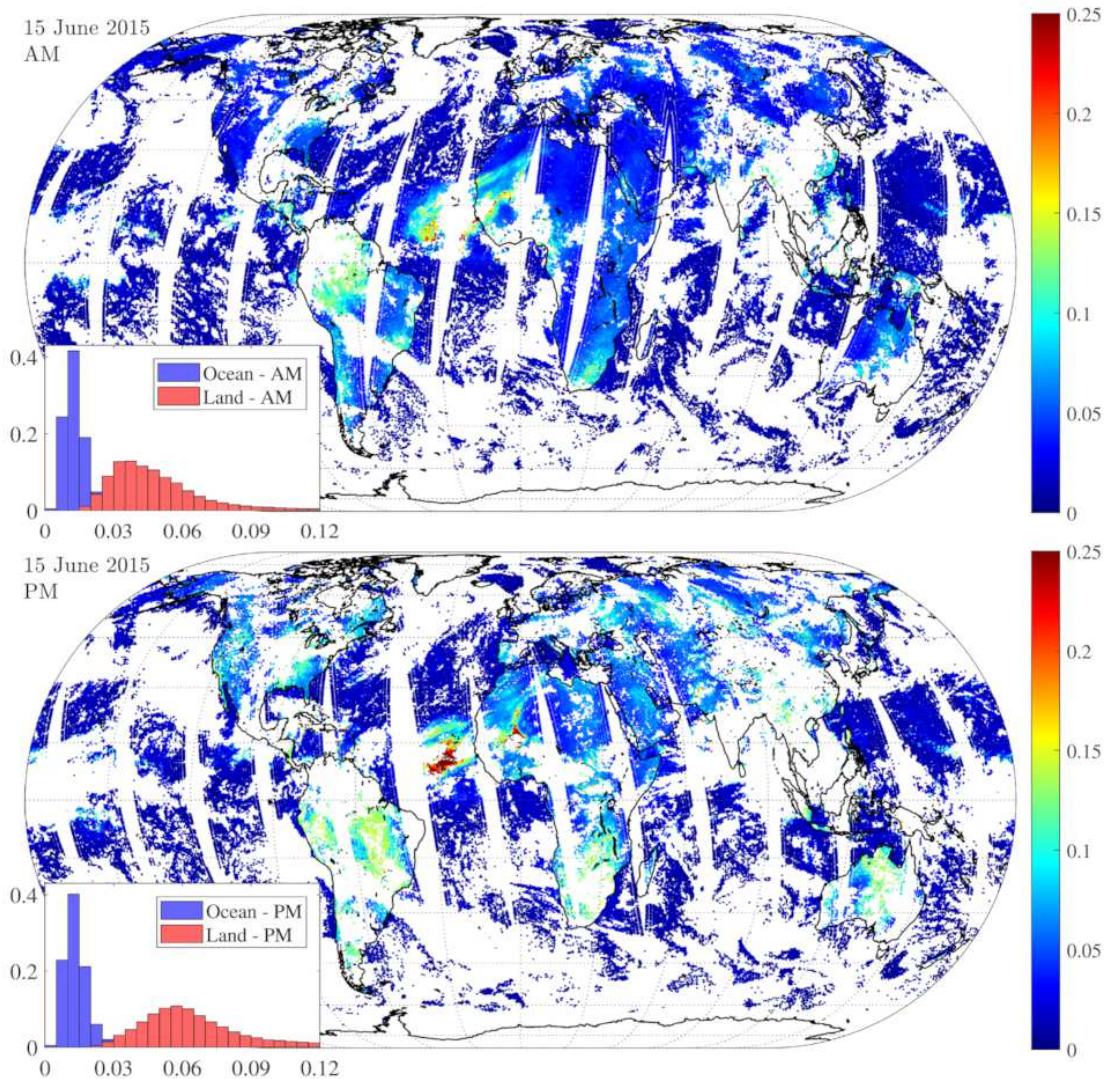


**Figure 4.12:** IASI-retrieved absolute OD uncertainties (unitless) for 15 June 2015 for the morning (top) and evening (bottom) overpass. The insets provide the probability histograms (frequency of each OD uncertainty values) of the global data.

## 4.2.4 Uncertainty characterisation

### 4.2.4.1 Systematic uncertainty

Systematic errors include biases introduced beyond our immediate control, due to the choice of the size distribution, refractive index and forward model. We have not carried out our own error analysis, but here we rely on studies from the LMD group (Pierangelo et al., 2004), since these in essence all stem from the forward model. The size distribution and refractive index were estimated to yield an error of maximum 10% each. Other forward model errors are expected to be negligible. In view of this we conservatively estimate our systematic error to be of the order of 25%.

#### 4.2.4.2 Random uncertainty

Here we discuss the uncertainty caused by uncertainties in the input parameters and input of the NN. The nature of the NN implies that we can very easily calculate how these errors propagate on the final OD retrieval. We attribute the following uncertainties  $\sigma$  to the five input parameters:

1. Aerosol altitude. Here we use the standard deviation of the CALIOP heights.  $\sigma_{ALT} = \sigma_{cal}$ .
2. IASI instrumental noise on R. The R-value, has by definition an uncertainty of  $\sigma_R = 1$ .
3. IASI instrumental noise on the input baseline channels. We use  $\sigma_{BL} = 0.28K$ .
4. Temperature profile. A value of  $\sigma_{TEMP} = 1$  K has been applied for the whole profile (Pougatchev et al., 2009, August et al., 2012).
5. Humidity profile. A value of  $\sigma_{HUM} = 10\%$  has been applied for the whole profile (Pougatchev et al., 2009, August et al., 2012).

In addition to these, there is the error caused by the imperfect training of the NN, this was set at  $\sigma_{NN} = 25\%$ . Using these we can calculate the total error on the OD as

$$\sigma_{OD} = \sqrt{\left(\frac{\partial OD}{\partial A} \sigma_{ALT}\right)^2 + \left(\frac{\partial OD}{\partial R} \sigma_R\right)^2 + \left(\frac{\partial OD}{\partial B} \sigma_{BL}\right)^2 + \left(\frac{\partial OD}{\partial T} \sigma_T\right)^2 + \left(\frac{\partial OD}{\partial H} \sigma_{HUM}\right)^2 + (\sigma_{NN})^2}$$

#### 4.2.5 Post-processing

At the end of the retrieval, the measurements are postprocessed to remove any clear erroneous retrievals or retrievals for which the measurement carries no meaningful information. A first criterion removes large negative retrievals, below a dust OD of  $-0.1$  or with an  $R$  value below  $-3$ . These are obvious candidates as their large unphysical value goes beyond the expected random noise. Next, all retrievals are removed for which the conversion ratio exceeds  $0.15$ , corresponding to conditions where the measurement sensitivity is extremely low. Finally, the observations are also flagged if both the absolute and relative uncertainty simultaneously exceed a threshold of  $0.15$  and  $50\%$ , respectively. The criterion on the absolute uncertainty is mostly relevant for observations with little or no detectable dust, while the criterion on the relative uncertainty is meaningful for observations with a detectable dust signature. As a whole, this postfiltering procedure keeps about  $98-99\%$  of the ocean measurements and about  $60-97\%$  of the land data (worst in the winter nighttime overpass, best in the summer daytime overpass).

## 5. REFERENCES

- August, T., Klaes, D., Schlüssel, P., Hultberg, T., Crapeau, M., Arriaga, A., O'Carroll, A., Coppens, D., Munro, R., & Calbet, X. 2012. IASI on Metop-A: Operational Level 2 retrievals after five years in orbit. *J. Quant. Spectrosc. Radiat. Transfer*, 113(11), 1340–1371.
- Camy-Peyret, C. & Eyre, J. 1998. The IASI Science Plan. Technical report, A Report From The IASI Sounding Science Working Group.
- Clarisse, L., Prata, F., Lacour, J.-L., Hurtmans, D., Clerbaux, C., & Coheur, P.-F. 2010a. A correlation method for volcanic ash detection using hyperspectral infrared measurements. *Geophys. Res. Lett.*, 37, L19806.
- Clarisse, L., Coheur, P.-F., Prata, F., Hadji-Lazaro, J., Hurtmans, D., & Clerbaux, C. 2013. A unified approach to infrared aerosol remote sensing and type specification. *Atmos. Chem. Phys.*, 13(4), 2195–2221.
- Clarisse, L., Hurtmans, D., Prata, A. J., Karagulian, F., Clerbaux, C., De Mazière, M., & Coheur, P.-F. 2010b. Retrieving radius, concentration, optical depth, and mass of different types of aerosols from high-resolution infrared nadir spectra. *Appl. Opt.*, 49(19), 3713–3722.
- Clarisse, L., Clerbaux, C., Franco, B., Hadji-Lazaro, J., Whitburn, S., Kopp, A., Hurtmans, D., & Coheur, P.-F. 2019. A decadal data set of global atmospheric dust retrieved from IASI satellite measurements. *J. Geophys. Res.: Atm.*, 124. <https://doi.org/10.1029/2018JD029701>
- Clerbaux, C., Boynard, A., Clarisse, L., George, M., Hadji-Lazaro, J., Herbin, H., Hurtmans, D., Pommier, M., Razavi, A., Turquety, S., Wespes, C., and Coheur, P.-F. 2009. Monitoring of atmospheric composition using the thermal infrared IASI/MetOp sounder. *Atmos. Chem. Phys.*, 9, 6041–6054.
- Delahaye, T., R. Armante, N.A. Scott, N. Jacquinet-Husson, A. Chédin, L. Crépeau, C. Crevoisier, V. Douet, A. Perrin, A. Barbe, V. Boudon, A. Campargue, L.H. Coudert, V. Ebert, J.-M. Flaud, R.R. Gamache, D. Jacquemart, A. Jolly, F. Kwabia Tchana, A. Kyuberis, G. Li, O.M. Lyulin, L. Manceron, S. Mikhailenko, N. Moazzen-Ahmadi, H.S.P. Müller, O.V. Naumenko, A. Nikitin, V.I. Perevalov, C. Richard, E. Starikova, S.A. Tashkun, V.I.G. Tyuterev, J. Vander Auwera, B. Vispoel, A. Yachmenev, S. Yurchenko, 2021. The 2020 edition of the GEISA spectroscopic database, *J. Mol. Spectrosc.* 380, 111510, <https://doi.org/10.1016/j.jms.2021.111510>.
- DeSouza-Machado, SG, Strow, LL, Hannon, SE, & Motteler, HE. 2006. Infrared dust spectral signatures from AIRS. *Geophys. Res. Lett.*, 33(3), L03801.
- Di Biagio, C., Formenti, P., Styler, S. A., Panguì, E., & Doussin, J.-F. 2014a. Laboratory chamber measurements of the longwave extinction spectra and complex refractive indices of African and Asian mineral dusts. *Geophys. Res. Lett.*, 41(17), 6289–6297.
- Di Biagio, C., Boucher, H., Caquineau, S., Chevaillier, S., Cuesta, J., & Formenti, P. 2014b. Variability of the infrared complex refractive index of African mineral dust: experimental estimation and implications for radiative transfer and satellite remote sensing. *Atmos. Chem. Phys.*, 14(20), 11093–11116.
- Fouquart, Y., Bonnel, B., Brogniez, G., Cerf, A., Chaoui, M., Smith, L., & Vanhouette, J. C. 1984. Size distribution and optical properties of Saharan aerosols during ECLATS. *Pages 35–62 of: Gerber, H. E., & Deepak, A. (eds), Aerosols and their Climatic Effects*. Hampton, Virginia: A. Deepak.
- Fouquart, Y., Bonnel, B., Brogniez, G., Buriez, J.C., Smith, L., & Morcrette, J.J. 1987. Observations of Saharan aerosols: results of ECLATS Field experiment. Part II: Broadband radiative characteristics of the aerosols and vertical radiative flux divergence. *J. Clim. Appl. Meteor.*, 26, 38–52.
- Gordon, I.E. et al. 2022. The HITRAN2020 molecular spectroscopic database. *J. Quant. Spectrosc. Radiat. Transf.* 277, 107949, <https://doi.org/10.1016/j.jqsrt.2021.107949>]
- Hess, M, Koepke, P, & Schult, I. 1998. Optical properties of aerosols and clouds: The software package OPAC. *Bull. Am. Meteorol. Soc.*, 79(5), 831–844.
- Hilton, F., August, T., Barnet, C., Bouchard, A., Camy-Peyret, C., Clarisse, L., Clerbaux, C., Coheur, P.-F., Collard, A., Crevoisier, C., Dufour, G., Edwards, D., Faijan, F., Fourrié, N., Gambacorta, A., Gauguin, S., Guidard, V., Hurtmans, D., Illingworth, S., Jacquinet-Husson, N., Kerzenmacher, T., Klaes, D., Lavanant, L., Masiello, G., Matricardi, M., McNally, T., Newman, S., Pavelin, E., Péquignot, E., Phulpin, T., Remedios, J., Schlüssel, P., Serio, C., Strow, L., Taylor, J., Tobin, D., Uspensky, A. and Zhou, D. 2012. Hyperspectral Earth Observation with IASI. *Bull. Am. Meteorol. Soc.*, 93(3), 347-370, doi: 10.1175/BAMS-D-11-00027.1.
- Hoidale, G.B., & Blanco, A.J. 1969. Infrared absorption spectra of atmospheric dust over an interior desert basin. *Pure Appl. Geophys.*, 74(1), 151–164.

- Hunt, G.R. 1982. Spectroscopic properties of rocks and minerals. Pages 295–385 of: Carmichael, R.S. (ed), *Handbook of physical properties of rocks*. Boca Raton, Florida: CRC.
- Hurley, J., Dudhia, A., & Grainger, R. G. 2009. Cloud detection for MIPAS using singular vector decomposition. *Atmos. Meas. Tech.*, 2(2), 533–547.
- Klüser, L., Martynenko, D., & Holzer-Popp, T. 2011. Thermal infrared remote sensing of mineral dust over land and ocean: a spectral SVD based retrieval approach for IASI. *Atmos. Meas. Tech.*, 4(5), 757–773.
- Nalli, N.R., Minnett, P.J., & van Delst, P. 2008. Emissivity and reflection model for calculating unpolarized isotropic water surface-leaving radiance in the infrared. I: Theoretical development and calculations. *Appl. Opt.*, 47(21), 3701–3721.
- Peters, D. 2009. *private communication*.
- Peyridieu, S., Chédin, A., Tanré, D., Capelle, V., Pierangelo, C., Lamquin, N., & Armante, R. 2010. Saharan dust infrared optical depth and altitude retrieved from AIRS: a focus over North Atlantic - comparison to MODIS and CALIPSO. *Atmos. Chem. Phys.*, 10, 1953–1967.
- Pierangelo, C, Chedin, A, Heilliette, S, Jacquinet-Husson, N, & Armante, R. 2004. Dust altitude and infrared optical depth from AIRS. *Atmos. Chem. Phys.*, 4, 1813–1822.
- Pougatchev, N., August, T., Calbet, X., Hultberg, T., Oduleye, O., Schlüssel, P., Stiller, B., Germain, K. S., & Bingham, G. 2009. IASI temperature and water vapor retrievals - error assessment and validation. *Atmos. Chem. Phys.*, 9(2), 6453–6458.
- Reid, J.S., Jonsson, H.H., Maring, H.B., Smirnov, A., Savoie, D. L., Cliff, S.S., Reid, E.A., Livingston, J. M., Meier, M. M., Dubovik, O., & Tsay, S.-C. 2003. Comparison of size and morphological measurements of coarse mode dust particles from Africa. *J. Geophys. Res.*, 108, 8593.
- Toon, O. B., Pollack, J. B., & Sagan, C. 1977. Physical properties of the particles composing the Martian dust storm of 1971-1972. *Icarus*, 30(4), 663–696.
- Tsamalis, C., Chédin, A., Pelon, J., & Capelle, V. 2013. The seasonal vertical distribution of the Saharan Air Layer and its modulation by the wind. *Atmos. Chem. Phys.*, 13(22), 11235–11257.
- Vandenbussche, S., Kochenova, S., Vandaele, A. C., Kumps, N., & De Mazière, M. 2013. Retrieval of desert dust aerosol vertical profiles from IASI measurements in the TIR atmospheric window. *Atmos. Meas. Tech.*, 6(10), 2577–2591.
- Volz, F. E. 1972a. Infrared Absorption by Atmospheric Aerosol Substances. *J. Geophys. Res.*, 77, 1017–1031.
- Volz, F. E. 1972b. Infrared Refractive Index of Atmospheric Aerosol Substances. *Appl. Opt.*, 11, 755–759.
- Volz, F. E. 1973. Infrared optical constants of ammonium sulfate, Sahara dust; volcanic pumice and flyash. *Appl. Opt.*, 12, 564–568.
- Volz, F. E. 1983. Infrared optical constants of aerosols at some locations. *Appl. Opt.*, 22(23), 3690–3700.
- Walker, J. C., Dudhia, A., & Carboni, E. 2011. An effective method for the detection of trace species demonstrated using the MetOp Infrared Atmospheric Sounding Interferometer. *Atmos. Meas. Tech.*, 4(5), 1567–1580.
- Whitburn, S., Clarisse, L., Crapeau, M., August, T., Hultberg, T., Coheur, P. F., & Clerbaux, C. 2022. A CO<sub>2</sub>-independent cloud mask from Infrared Atmospheric Sounding Interferometer (IASI) radiances for climate applications, *Atmos. Meas. Tech.*, 15, 6653–6668, <https://doi.org/10.5194/amt-15-6653-2022>.
- Yu, H., Chin, M., Winker, D. M., Omar, A. H., Liu, Z., Kittaka, C. & Diehl, T. 2010. Global view of aerosol vertical distributions from CALIPSO lidar measurements and GOCART simulations: Regional and seasonal variations. *J. Geophys. Res.*, 115(D4), D00H30.
- Zhou, D. K., Larar, A. M., & Liu, X. 2013. MetOp-A/IASI Observed Continental Thermal IR Emissivity Variations. *IEEE J. Sel. Topics Appl. Earth Observations Remote Sens.*, 6(3), 1156–1162.
- Zhou, D.K., Larar, A.M., Liu, X., Smith, W.L., Strow, L.L., Yang, P., Schlüssel, P., & Calbet, X. 2011. Global Land Surface Emissivity Retrieved From Satellite Ultraspectral IR Measurements. *IEEE T. Geosci. Remote.*, 49, 1277–1290.